Phase measurement of a segmented wave front using PISton and TILt interferometry (PISTIL)

Maxime Deprez, Benoit Wattellier, Cindy Bellanger, Laurent Lombard, Jerôme Primot

Research Article | Vol. 26, No. 5 | 5 Mar 2018 | OPTICS EXPRESS 5212
Optics EXPRESS

Phase measurement of a segmented wave front using PIston and TILt interferometry (PISTIL)

MAXIME DEPREZ,[1,2,*] BENOIT WATTELLIER,[1] CINDY BELLANGER,[2] LAURENT LOMBARD,[2] AND JÉRÔME PRIMOT[2]

[1]*Phasics SA, Bâtiment Explorer Parc Technologique de Saint-Aubin, Route de l'Orme des Merisiers, 91190 Saint-Aubin, France*
[2]*ONERA–The French Aerospace Lab, F-91761 Palaiseau, France*
**maxime.deprez@onera.fr*

Abstract: New architectures for telescopes or powerful lasers require segmented wave front metrology. This paper deals with a new interferometric wave front sensing technique called PISTIL (PIston and TILt), able to recover both piston and tilts of segment beams. The main advantages of the PISTIL technique are the absence of a reference arm and an access to the tilt information. An explanation of the principle, as well as an experimental implementation and the use of a segmented active mirror, are presented. Measurement errors of λ/200 for piston and 40 µrad for tilts have been achieved, well beyond performances requested for the above mentioned applications.

OCIS codes: (010.1080) Active or adaptive optics; (010.7350) Wave-front sensing; (120.3180) Interferometry; (120.5050) Phase measurement; (140.3298) Laser beam combining; (350.1260) Astronomical optics.

References and links

1. https://www.eso.org/sci/facilities/eelt
2. G. Chanan, M. Troy, F. Dekens, S. Michaels, J. Nelson, T. Mast, and D. Kirkman, "Phasing the mirror segments of the Keck telescopes: the broadband phasing algorithm," Appl. Opt. **37**(1), 140–155 (1998).
3. G. Mourou, B. Brocklesby, T. Toshiki, and J. Limpert, "The future is fiber accelerators," Nat. Photonics **7**(4), 258–261 (2013).
4. M. Deprez, C. Bellanger, L. Lombard, B. Wattellier, and J. Primot, "Piston and tilt interferometry for segmented wavefront sensing," Opt. Lett. **41**(6), 1078–1081 (2016).
5. K. Dohlen, M. Langlois, P. Lanzoni, S. Mazzanti, A. Vigan, L. Montoya, E. Hernandez, M. Reyes, I. Surdej, and N. Yaitskova, "ZEUS: a cophasing sensor based on the Zernike phase contrast method," Proc. SPIE **6267**, 626734 (2006).
6. S. Esposito, E. Pinna, A. Puglisi, A. Tozzi, and P. Stefanini, "Pyramid sensor for segmented mirror alignment," Opt. Lett. **30**(19), 2572–2574 (2005).
7. T. K. Korhonen, "Interferometric method for optical testing and wavefront error sensing," Proc. SPIE 0444, Advanced Technology Optical Telescopes I (1983).
8. R. Penrose and J. A. Todd, "A generalized inverse for matrices," Math. Proc. Camb. Philos. Soc. **51**(3), 406–413 (1955).
9. M. G. Löfdahl and H. Eriksson, "Algorithm for resolving 2π ambiguities in interferometric measurements by use of multiple wavelengths," Opt. Eng. **40**(6), 984–990 (2001).
10. B. Toulon, J. Primot, N. Guérineau, R. Haïdar, S. Velghe, and R. Mercier, "Step-selective measurement by grating-based lateral shearing interferometry for segmented telescopes," Opt. Commun. **279**(2), 240–243 (2007).
11. M. Takeda, H. Ina, and S. Kobayashi, "Fourier-transform method of fringe-pattern analysis for computer-based topography and interferometry," J. Opt. Soc. Am. **72**(1), 156–160 (1982).
12. J.-C. Chanteloup and M. Cohen, "Compact high resolution four wave lateral shearing interferometer," Proc. SPIE **5252**, 5252 (2004).
13. W. H. Southwell, "Wave-front estimation from wave-front slope measurements," J. Opt. Soc. Am. **70**(8), 998–1006 (1980).
14. http://www.irisao.com/
15. http://www.jai.com
16. A. Helmbrecht, T. Juneau, M. Hart, and N. Doble, "Performance of a high-stroke segmented MEMS deformable-mirror technology," Proc. SPIE **6113**, 61130L (2006).
17. R. K. Tyson, M. Scipioni, and J. Viegas, "Generation of an optical vortex with a segmented deformable mirror," Appl. Opt. **47**(33), 6300–6306 (2008).

#309954 https://doi.org/10.1364/OE.26.005212
Journal © 2018 Received 17 Nov 2017; revised 19 Jan 2018; accepted 20 Jan 2018; published 21 Feb 2018

Optics EXPRESS

18. A. Norton, D. Gavel, and D. Dillon, "High-power visible-laser effect on a 37-segment Iris AO deformable mirror," Proc. SPIE **7595**, 759506 (2010).
19. http://phasicscorp.com/
20. J. Le Dortz, A. Heilmann, M. Antier, J. Bourderionnet, C. Larat, I. Fsaifes, L. Daniault, S. Bellanger, C. Simon Boisson, J.-C. Chanteloup, E. Lallier, and A. Brignon, "Highly scalable femtosecond coherent beam combining demonstrated with 19 fibers," Opt. Lett. **42**(10), 1887–1890 (2017).
21. L. Daniault, S. Bellanger, J. Le Dortz, J. Bourderionnet, E. Lallier, C. Larat, M. Antier-Murgey, J.-C. Chanteloup, A. Brignon, C. Simon-Boisson, and G. Mourou, "XCAN – A coherent amplification network of femtosecond fiber-chirped-pulse amplifiers," Eur. Phys. J. Spec. Top. **224**(13), 2609–2613 (2015).

1. Introduction

New applications using segmented wave fronts appeared recently in several projects. One is the new generation of telescopes for astronomy where one of the best known is the E-ELT [1]. Composed by segmented mirrors (up to 800), the reconstituted primary mirror need a step of co-phasing [2] to retrieve a high quality image. Other field where segmented wave fronts emerge is the new generation of high energy and high repetition rate lasers based on the combination of smaller individually amplified laser fibers as proposed, for example, for LaserWakeField Acceleration (LWFA) [3]. These two applications require a wave front sensor to measure pistons and tilts of a wave front segmented into a Hexagonal or Cartesian mesh. Due to the difference between astronomy field (turbulence, few photons) and laser field (negligible high orders, high power), this paper will be focus on coherent combining of fibers.

In particular case of laser field, the set-up must be fast, typically in the kHz range, to reach a real-time correction. It must also address a high dynamic range, up to 100 λ with a piston measurements error below λ<60 and a tip/tilt measurements error below 0.3mrad, assuming the absence of high orders.

In this article, we present an interferometer called PISTIL [4] (PISton and TILt) which can be used to measure both absolute pistons (using λ disambiguations), and tip/tilt of a periodically segmented wave front using a simple interference pattern analysis. PISTIL interferometer is highly scalable, and does require any reference beam [5–7]. Measurements can be operated at kHz rate thanks to the simplicity of the pattern analysis. The paper is outlined as follows. In section 2 we describe the principle of PISTIL interferometer; in section 3 the experimental implementation and in section 4, we present and discuss experimental results.

2. Piston and tilt interferometry description

PISTIL principle

The principle of PISTIL interferometer is to measure a periodically segmented wave front from phase differences between segment couples. To do so, we replicate the segmented wave fronts with a diffractive optic and make the replicas overlap and interfere two by two. The obtained interference patterns lead to phase difference, which are then integrated to recover the whole absolute wave front.

The first step is to lacunarize the wave front using a well-adjusted hole mask that selects only the center part of each segments of the wave front, see Fig. 1. This is necessary to ensure that the signal on each overlapping zones contains information about only two adjacent segments. Therefore the hole diameter must be lower than half the distance between the centers of two adjacent segments. The resulting wave front is then going through a diffraction grating that creates lateral sheared replicas of the incident wave front. The grating geometry is designed so that the diffraction directions correspond to the segment grid Bravais lattice, an additional replica from zero order can be kept for intensity information. For example, with a Cartesian grid, we choose a grating that creates four replicas, with a hexagonal one, we create 6 replicas. After a certain distance of propagation, we obtain a perfect overlap between replicas of adjacent segments, see Fig. 2. They interfere and the resulting fringes are acquired by a camera. They carry the information of phase difference between adjacent segments. In

Optics EXPRESS

particular we recover the relative piston and tip/tilt between two adjacent sub-wave fronts. The complete segmented surface can then be retrieved by integration of these differences.

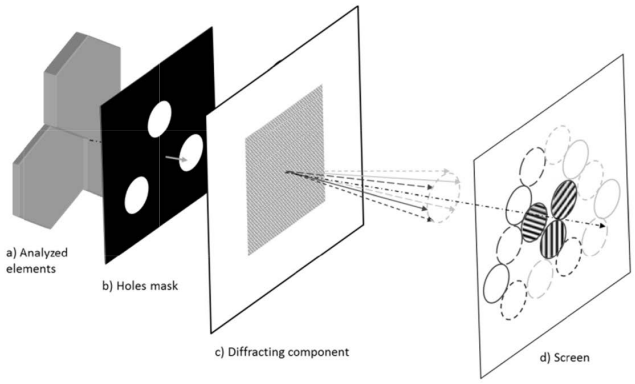

Fig. 1. Schematic view of PISTIL technic with 3 elements in hexagonal mesh.

For more convenience, afterwards, the interferogram will be called “pistilogram”, and the fringe pattern in one overlapping zone will be called “petal”.

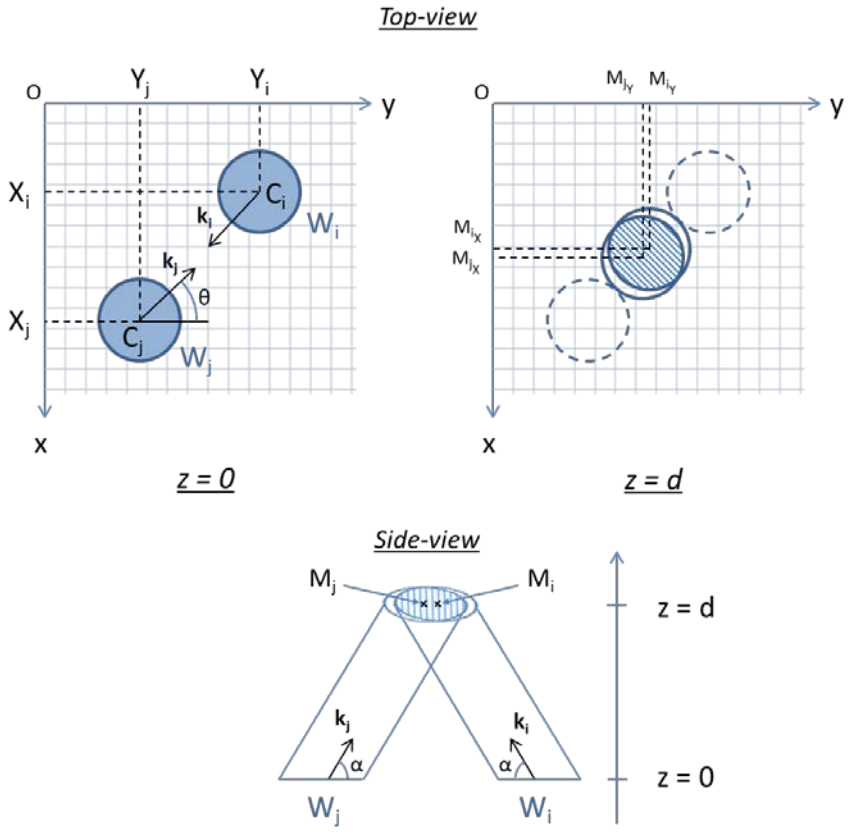

Fig. 2. Description of two-wave interference due to lateral shearing with two plan segmented wave fronts. Top left: two plan wave fronts Wi and Wj at z = 0 (just before propagation through the grating). Top right: interference fringe pattern after a propagation.

Optics EXPRESS

Recorded signal derivation

To compute the fringe intensity expression on a petal, we consider two sub-wave fronts W_i and W_j from the whole segmented wave front, emerging from the hole mask, see Fig. 2).

Two replicas are created by propagation through the grating situated in the plan (Oxy). Their wave vectors $\mathbf{k_{i/j}}$ are defined as follow Eq. (1):

$$\overrightarrow{k_i} = \begin{pmatrix} -\alpha \sin\theta \\ \alpha \cos\theta \\ 1 \end{pmatrix}, \overrightarrow{k_j} = \begin{pmatrix} \alpha \sin\theta \\ -\alpha \cos\theta \\ 1 \end{pmatrix} \tag{1}$$

α in Fig. 2 at bottom is obtained from the grating formula in transmission with perpendicular incident plane wave (Eq. (2,3)) and θ (Eq. (4)) is related to the geometry of the grating in Fig. 2 at top left, so it is common for all sub-wave fronts emerging from the hole mask:

$$\sin(\alpha) = \frac{m\lambda}{p_g} \tag{2}$$

p_g is the grating period in the Bravais lattice. We can consider $\alpha << 1$ and $m = 1$ (first order), so α becomes Eq. (3):

$$\alpha \cong \frac{\lambda}{p_g} \tag{3}$$

And θ is defined by Eq. (4):

$$\cos(\theta) = \frac{\overrightarrow{k_i}.\overrightarrow{Oy}}{\left\| \overrightarrow{k_i}.\overrightarrow{Oy} \right\|} \tag{4}$$

Therefore, the lateral shearings $\mathbf{s_{i/j}}$ Eq. (5) at $z = d$ are equal to:

$$\overrightarrow{s_i} = d\overrightarrow{k_i} = \begin{pmatrix} -d\,\lambda/p_g \sin\theta \\ d\,\lambda/p_g \cos\theta \\ d \end{pmatrix}, \overrightarrow{s_j} = d\overrightarrow{k_j} = \begin{pmatrix} d\,\lambda/p_g \sin\theta \\ -d\,\lambda/p_g \cos\theta \\ d \end{pmatrix} \tag{5}$$

The complex field for one wave front is described as follow:

$$U_i^{\lambda}(x,y,z) = U_{i_0}(x,y) \times \exp\left(i\frac{2\pi}{\lambda}\overrightarrow{k_i}.\vec{r} + i\frac{2\pi}{\lambda}W_i\left(\vec{r} - \overrightarrow{s_i}\right)\right) \tag{6}$$

where $U_{i0}(x,y)$ represent the amplitude, r the unit vector, and W_i the wave front with lateral shearing s_i.

In first approximation, we suppose that $U_{i0} = U_{j0} = U_0$. After calculation, the intensity on the camera, resulting of the two-wave interference field (U_i^{λ} and U_j^{λ}), becomes Eq. (7):

$$I_{ij}^{\lambda}(x,y,z) = 2I_0 + 2I_0 \cos\left(\frac{2\pi}{\lambda}\left(\overrightarrow{k_i} - \overrightarrow{k_j}\right).\vec{r} + \frac{2\pi}{\lambda}\left(W_i\left(\vec{r} - \overrightarrow{s_i}\right) - W_j\left(\vec{r} - \overrightarrow{s_j}\right)\right)\right) \tag{7}$$

In the scope of this article, we assume that both sub-wave fronts W_i and W_j are flat. Hence they are uniquely described by the position of their center, respectively $\mathbf{C_{i/j}}$ $(X_{i/j}, Y_{i/j}, 0)$ in the

Optics EXPRESS

orthonormal coordinate system (O,x,y,z), their tip/tilt angles $t_{Xi/j}$ and $t_{Yi/j}$ and the piston phase $A_{i/j}$.

The wave front equations are thence equal to Eq. (8):

$$\begin{aligned} W_i(x,y,z) &= t_{X_i}(x-X_i)+t_{Y_i}(y-Y_i)+A_i+o\left(x^n,y^n\right) \\ W_j(x,y,z) &= t_{Xj}(x-X_j)+t_{Y_j}(y-Y_j)+A_j+o\left(x^n,y^n\right) \end{aligned} \tag{8}$$

$o(x^n,y^n)$ represents the residual wave front (curvature, astigmatism) with n>1 that is neglected in our approach. Within this assumption, Eq. (7) simplifies to Eq. (9):

$$I_{ij}^{\lambda}(x,y,z) = 2I_0 + 2I_0\cos\left(2\pi\left(\begin{array}{c}\left(\frac{2\sin\theta}{p_g}+\frac{dt_{X_{ij}}}{\lambda}\right)x \\ +\left(\frac{-2\cos\theta}{p_g}+\frac{dt_{Y_{ij}}}{\lambda}\right)y \\ +\frac{1}{\lambda}\left(t_{X_i}M_{i_X}-t_{X_j}M_{j_X}+t_{Y_i}M_{i_Y}-t_{Y_j}M_{j_Y}+dP_{ij}\right)\end{array}\right)\right) \tag{9}$$

where $M_{i/jx}$ and $M_{i/jy}$ (Eq. (10)) are the positions of the replicated and translated centers in plane $z = d$, see Fig. 2.

$$\begin{aligned} \overrightarrow{M_i} &= \overrightarrow{C_i}+\overrightarrow{s_i} = \begin{pmatrix} X_i \\ Y_i \\ 0 \end{pmatrix} + \begin{pmatrix} -d\,\lambda/p_g\,\sin\theta \\ d\,\lambda/p_g\,\cos\theta \\ d \end{pmatrix} \\ \overrightarrow{M_j} &= \overrightarrow{C_j}+\overrightarrow{s_j} = \begin{pmatrix} X_j \\ Y_j \\ 0 \end{pmatrix} + \begin{pmatrix} d\,\lambda/p_g\,\sin\theta \\ -d\,\lambda/p_g\,\cos\theta \\ d \end{pmatrix} \end{aligned} \tag{10}$$

We also have $dt_{Xij} = t_{Xi} - t_{Xj}$, $dt_{Yij} = t_{Yi} - t_{Yj}$ and $dP_{ij} = A_i - A_j$.

In practice, the interferometer is aligned and the pupil centers are defined so that the third term between brackets in Eq. (9) reduces to dP_{ij}.

Finally, we can rewrite the intensity in the form of Eq. (11):

$$I_{ij}^{\lambda}(x,y,z) = 2I_0 + 2I_0\cos(ax+by+\Delta\varphi) \tag{11}$$

a, b and $\Delta\varphi$ are defined by Eq. (12):

$$\begin{aligned} a &= 2\pi\left(\frac{2\sin\theta}{p_g}+\frac{dt_{X_{ij}}}{\lambda}\right) \\ b &= 2\pi\left(\frac{-2\cos\theta}{p_g}+\frac{dt_{Y_{ij}}}{\lambda}\right) \\ \Delta\varphi &= 2\pi\frac{dP_{ij}}{\lambda} \end{aligned} \tag{12}$$

Optics EXPRESS

As we can see on the animation in Fig. 3, piston in segment 1 shifts the fringe pattern $I_{ij}^{\lambda}(x,y)$ as it introduces a phase shift in the cosine. Tip/tilt in segment 1 modifies the fringe carrier-frequency, so their spacing is altered. Particularly, if we look at fringes between segment 7 and 1 $I_{17}^{\lambda}(x,y)$, and segment 1 and 4 $I_{14}^{\lambda}(x,y)$, a tip changes only the carrier-frequency and a tilt changes only the fringe orientation.

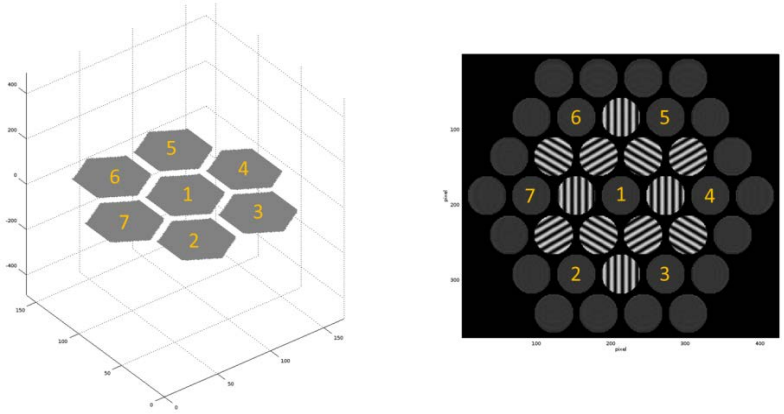

Fig. 3. Piston and tip/tilt impact on fringes (see Visualization 1).

Analyzing the fringe pattern on each petal leads to relative piston/tip/tilt information (dP_{ij}, dt_{Xij}, dt_{Yij}) between two adjacent wave fronts. Retrieving the absolute surface needs an integration of the information for each wave front couples. This can be done by a well-adapted least square method (Moore-Penrose [8] for example).

We see from Eq. (11) that any phase-shift larger than π (or λ/2) will be wrapped back to the [-π;π] range. To remove this ambiguity, we can use a multi-color technique where measurements at different wavelengths are combined. This increases the instrument dynamic range [9, 10].

Pistilogram computing method

Phase retrieval from a recorded pistilogram is a standard problem, where a signal is encoded in a frequency modulation. For the proof of principle, we used a standard Fourier Transform method [11, 12].

In a first step, we Fourier transform the pistilogram Eq. (13), filter each useful harmonic (with Hamming filter for example), and finally inverse Fourier transform the selected harmonic. The argument of the obtained complex field is the phase difference between both segments which interfered in the petal.

$$TF\left[I_{ij}^{\lambda}(x,y,z)\right] = 2\tilde{I}_0 + 2\tilde{I}_0 \times \left[\delta\left(\upsilon_x - \frac{a}{2\pi}\right)\delta\left(\upsilon_y - \frac{b}{2\pi}\right)\exp\left(-2i\pi\Delta\varphi\right) + c.c.\right] \quad (13)$$

Slopes and offset of this phase difference are directly related respectively to relative tip/tilt (dt_{Xij}, dt_{Yij}) and piston (dP_{ij}) between W_i and W_j. One way to retrieve those values is to fit the retrieved phase difference with an affine plane equation.

Figure 4 shows a superposition of phase petal coming from several harmonic. In this example, central segment present a piston of λ/10.

Optics EXPRESS

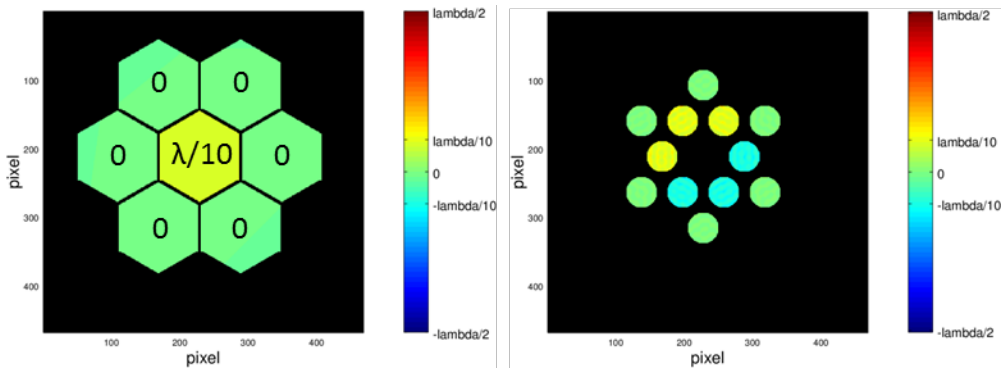

Fig. 4. Left, values of the phase shifts within segments; right, example of reconstituted relative phase difference image from typical pistilogram obtained in Fig. 3.

So, throughout the rest of the document, we will examine only relative piston which will be between –λ/2 and λ/2. As explained in section 2, this method gives access to the piston/tip/tilt relationship between two adjacent sub-wave fronts. The retrieval of the whole segmented surface has been realized by integration of the measurements with a mean square method. The redundancy information is used to improve the robustness of the measure [13].

3. Experimental implementation

Experimental setup

Figure 5 shows a scheme of the experimental setup that we used to evaluate the performances of PISTIL technique towards the segmented wave front from a segmented mirror.

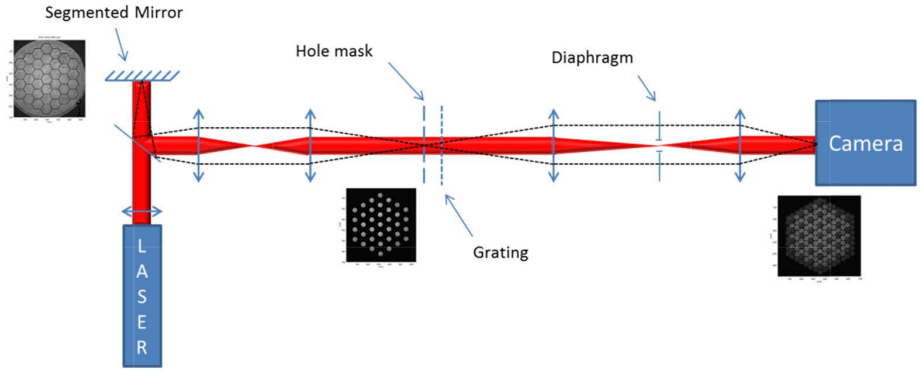

Fig. 5. Experimental setup with segmented mirror and high speed camera.

We use a collimated laser diode from Qphotonics (QFLD-980-50S-PM) with a wavelength of 980nm that illuminate the segmented mirror from IRIS AO [14] described hereafter. The deformable mirror is next imaged onto a holes mask with a first afocal system (magnification 1). The holes mask has the same hexagonal geometry as the deformable mirror with a pitch of 606µm, with hole diameters of 300µm. After the hole mask, the segmented wave front is imaged on a camera from JAI [15] (SP-5000-CXP4, 2580 × 2048pixel^2, pixel pitch = 5 × 5µm^2) with a second afocal system (magnification 0.75). To create the desired pistilogram, we place the grating (binary DOE phase in hexagonal mesh with a pitch of 112µm, keeping zero order information) just after the holes mask. A photo of the setup is shown in Fig. 6.

Optics EXPRESS

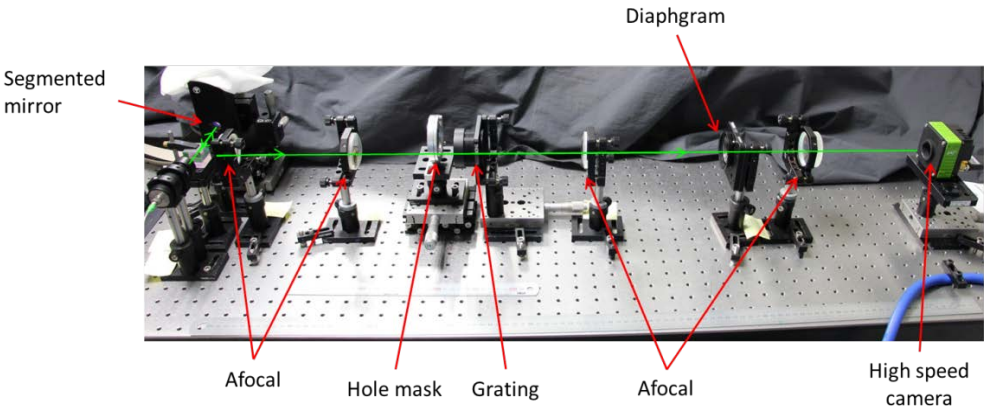

Fig. 6. Photo of the experimental setup.

One can note that the experimental configuration of the PISTIL interferometer is somehow different from the scheme described in Fig. 1. Indeed, we add two afocal systems for practical reasons. Because of the symmetry of diffraction order, the result is identical. So the optimal distance described in the section 2 is here the distance between the holes mask and the grating. Also, a pinhole can be place in the Fourier plane of the second afocal to filter out higher orders of the grating.

The resulting pistilogram is described in Fig. 7:

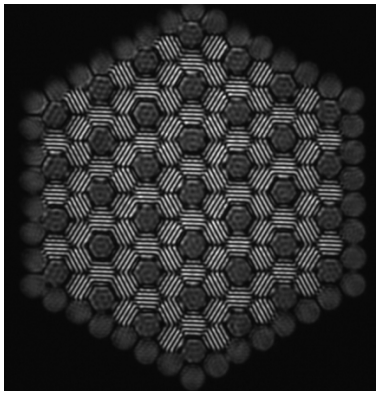

Fig. 7. Experimental pistilogram generate with previous setup.

The size of a typical pistilogram we obtained is 698 × 704 pixels^2 (3.49 × 3.52mm^2). The diameter of a petal is around 35 pixels and contains around 5 fringes.

Segmented deformable mirror characterization

To test the relevance of PISTIL technique in measuring segmented wave fronts as specified in section 1, we used a segmented deformable mirror that we precisely characterized.

In our setup, we used a mirror from IRIS AO (IAO-PTT111-5-SDMS) that is composed of 37 hexagonal segments with a diameter of 700µm arranged in a hexagonal mesh. On each segment, piston can be applied from –2.5µm to 2.5µm and tip/tilt angles between –5 mrad and 5 mrad up to 6.5kHz rates. The MEMS technology has a high precision [16] and IRIS AO deformable mirror have been used in other application with good performances [17, 18]

The segmented mirror was characterized by a commercial wave front sensor from Phasics [19] (SID4 with an aperture of 3,6 × 4,8mm^2) in pistons and tilts for each individual segment at 635nm. We found that:

Optics EXPRESS

- In piston, values in the range [-2000nm ; 2000nm] are correctly reached by small mirrors. Measured values of piston are proportional to the setpoint values with a slope of 0.983.

- In tilt, we saw that the segment accurately reaches the setpoint for tip in the range [-2mrad; 2 mrad], and tilt [-1mrad; 1mrad]. Higher value setpoints are not reached.

In respect to specifications in section 1, this deformable mirror will perfectly satisfy its mission to simulate the applications and test the PISTIL technique.

4. Results

We will present three kinds of measurements:

- Resolution and repeatability of the technique

- Piston only measurements

- Tip/tilt and piston measurement

4.1 Resolution and repeatability system measurement

To determine the resolution and repeatability limit of our technique, we acquired 100 pistilograms at the rate of 931Hz with the piston setpoint set to zero for all segments. We then measure the variation of absolute piston and tip/tilt. To do so, we consider the first pistilogram as a reference, and we compare all the others with it. The piston resolution is defined here as the standard deviation calculated for the 37 piston errors when the setpoint is zero. The same definition is used for tip and tilt.

We find a piston resolution around 0.18nm (λ/5400), and a tilt resolution of 2.5µrad. This resolution contains a contribution due to the environment (vibration, thermic effect, air flow, etc.), a contribution from the mirror and a contribution from the measurement itself.

The repeatability represents the capability of a system to reproduce the same state through several measurements without any changes, under the same conditions in a short period of time. In our case, the repeatability is quantified by the dispersion of segment measurements.

To measure the repeatability, we examine the central segment of the deformable mirror. We test 5 values of piston (–100nm, –50nm, 0nm, 50nm and 100nm) successively, and repeat this sequence ten times each. For each values of piston, the repeatability is computed by the standard deviations of the 10 results. So, we have 5 values of repeatability that we mean to obtain the mean repeatability in piston. We adopt the same scheme for the tip (–500µrad, –200 µrad, –100 µrad, 0 µrad, 100 µrad, 200 µrad, 500µrad), and the tilt (–500µrad, –200 µrad, –100 µrad, 0 µrad, 100 µrad, 200 µrad, 500µrad). We compute also the mean repeatability for tip/tilt.

The mean repeatability in piston is 0.54nm (λ/1814) and the mean repeatability in tip/tilt is 9.9µrad.

4.2 Measurement with only piston

We generated 100 pistilograms with 100 random setpoints sent to the deformable mirror. A sample result is shown in Fig. 8:

Optics EXPRESS

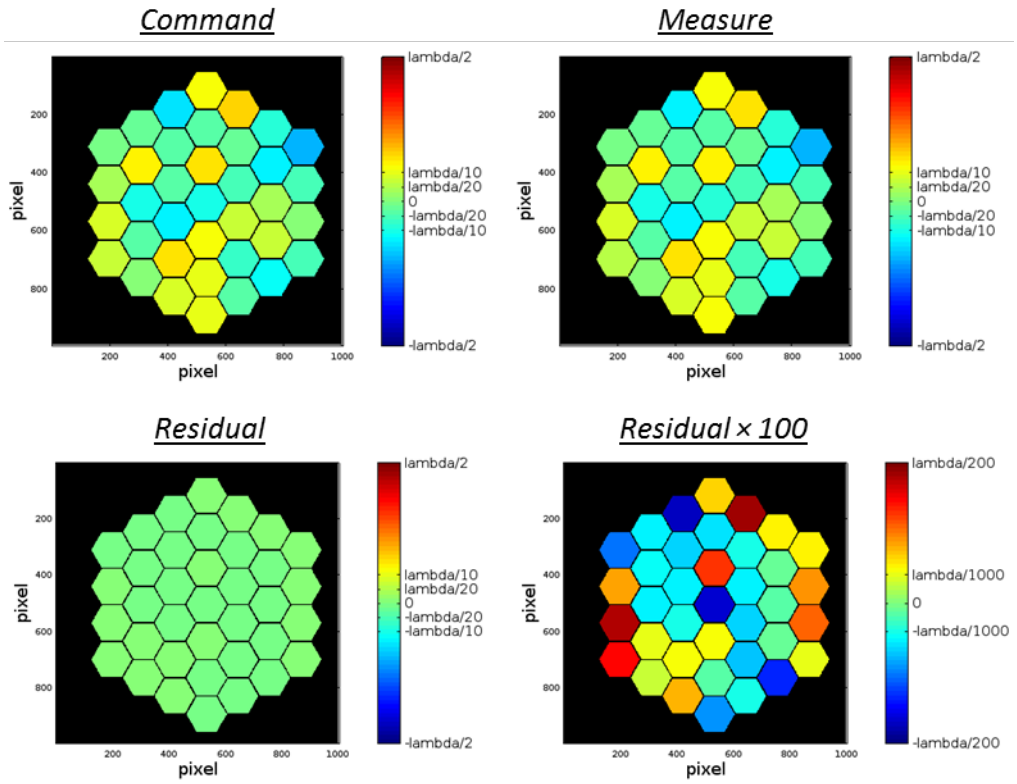

Fig. 8. Top left: command sent to the mirror. Top right: Measure with PISTIL interferometer. Bottom left: Residual (difference between top right and top left). Bottom right: Residual zoomed by 100.

If we look at segment by segment, we can see that the maximum segment error is below λ/200.

To determine the piston error, we calculate the standard deviation of the 37 absolute piston differences. So, the 37-segments-standard-deviation averaged over the 100 pistilograms is 1.94nm (λ/505). A first explication to this value is the resolution positioning segment provided by the manufacturer of the segmented mirror, which is in the order of 2nm. That's why it may be greater than the resolution determined in 4.1.

4.3 Measurement with piston and tilt

In this experience, we add a random tip/tilt with the random piston and acquire 100 new pistilograms. On each pistilograms, standard deviation of the errors (difference between setpoint and measured value) is evaluated separately in piston and tilts. We can see in the movie Fig. 9:

Optics EXPRESS

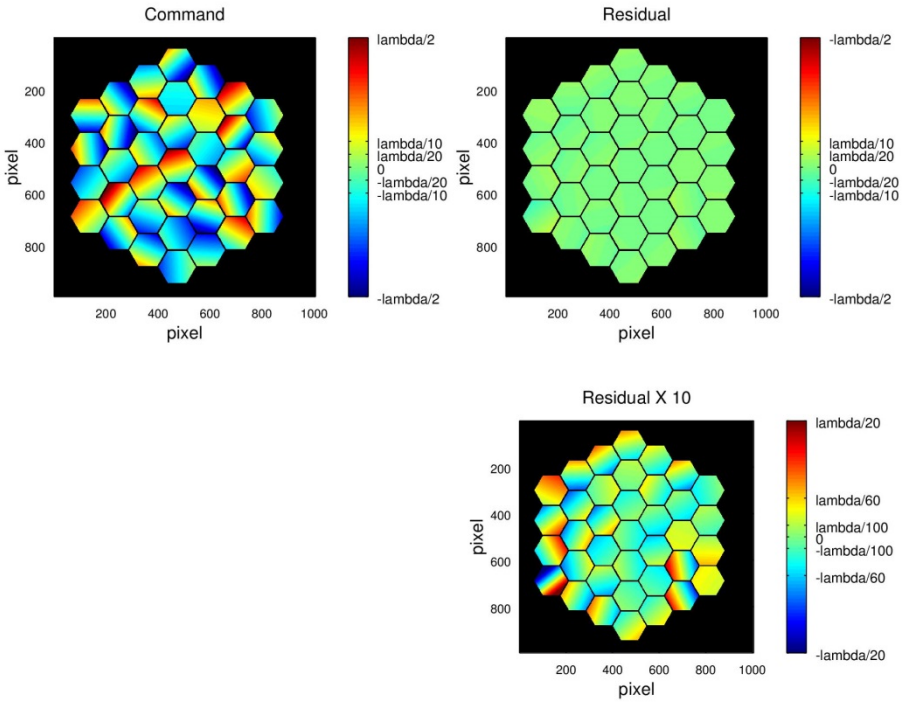

Fig. 9. In the left hand side, the command sent to the deformable mirror, at right the residual between the measure and the command, and at the bottom the residual zoomed by 10 (see Visualization 2).

The 37-segments-standard-deviation averaged over the 100 realizations is around 5.7nm ($\lambda/172$) and around 39µrad for the piston and tilts respectively. The piston error standard deviation is clearly higher than the measurements in 4.2. (1.98nm). We suspect that this is due to the displacement of the small mirrors of the segmented mirror. Indeed, a small mirror is piloted by 3 actuators which provide the command in piston and tip/tilt. Small mirrors may not reach some piston/tip/tilt configuration determined by the step of each actuator.

This minimal step corresponds to 1 LSB (Least Significant Bit) available for one actuator. Supplementary tests have been made with short change of piston setpoints, between –5 nm and 5 nm with 0.25 nm step, to verify it. Results are shown in Fig. 10.

Optics EXPRESS

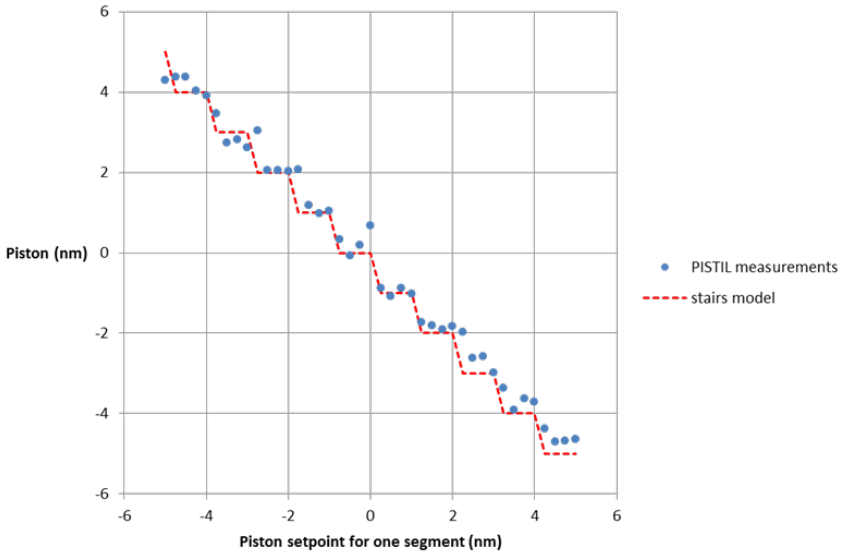

Fig. 10. Measurements done with small variations in piston for one segment

Measurements done with PISTIL technique seems to fit with a stairs model where we suppose that the LSB is around 1 nm.

Additional measurements done on a small range in tilt did not give the stairs effect, probably because we are under the resolution of the interferometer.

The actuators minimal step may explain the higher value in piston, and also the value in tip/tilt higher than the resolution and repeatability of the system.

4.4 Linearity of the system

Measurements of section 4.2 have been used to test the linearity of PISTIL technique. Indeed, we tested all segments at different values of piston. In MEMS technology, there is a quadratic relationship between applied voltage and segment piston. A previous calibration is done in factory for the user in order to have a linear response. So the plot of measurements versus setpoint sent to the segmented mirror in Fig. 11 will give us directly the linearity of segments.

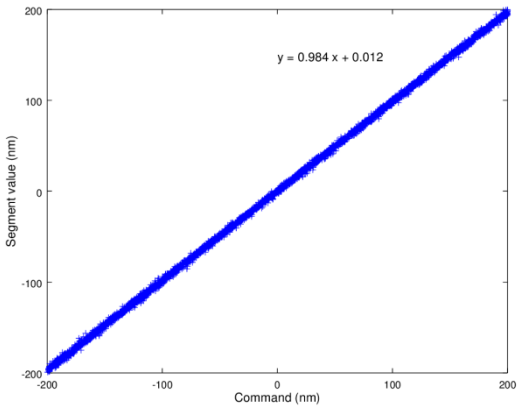

Fig. 11. Representation of measurements of pistons for all segments according to commands sent to the mirror. Regression fit is shown on the plot.

Optics EXPRESS

The slope in Fig. 11 is 0.984. This value is in good agreement with the value obtained with the SID4 characterization (section 3) of 0.983.

Same thing has been realized with piston values of measurements of section 4.3 where we find a slope of 0.983 which is also in agreement with previous values.

The slope value should be 1 but it is measured around 0.984 with two independent sensors (PISTIL and SID4). This could be a calibration error of the mirror itself (actual piston vs. setpoint piston).

5. Conclusion and discussion

We investigate the PISTIL interferometer dedicated to the measurement of periodically (hexagonal or cartesian) segmented wave fronts. With no reference arm, we are able to measure mean piston and also mean tip/tilt of each aperture. The interferogram only shows patterns resulting from two-wave interference. The technique has been tested on a segmented deformable mirror, composed of 37 independent segments that can be moved in piston and tip/tilts.

The main results are summarized in the following table:

Table 1. Noise, repeatability and measurement error in case of piston and tilt for PISTIL interferometer

	Piston	Tilt (µrad)
Noise	λ/5000	2.5
Repeatability	λ/1800	9
Measurement error (Piston only)	λ/500	
Measurement error (Piston and tilt)	λ/200	40

Further work includes implementing multi lambda measurements to increase the dynamic in piston measurements and an optimized pistilogram algorithm retrieval method for better efficiency and speed. Further studies will be done to adapt the interferometer in particular case of co-phasing telescope segmented mirrors, particularly the loss of high orders information or the effect of the turbulence on the interferogram.

Taking into account the metrological results presented in Table 1, we estimate that PISTIL interferometer has reached a sufficient maturity to be tested on XCAN demonstrator [20,21]. This laser system is based on the coherent combination of several tens of femtosecond laser beams produced through a network of amplifying optical fibers. Our measurement bench is now implemented on XCAN and first results on a 61 lasers combination are expected early 2018.

Funding

“Investissements d’Avenir” LabEx PALM (ANR-10-LABX-0039-PALM); PISTIL project; Phasics; ANRT.

Acknowledgments

The authors want to thank XCAN project team, for their precious help in the validation of the interferometer.